Tailoring the thermal conductivity in nanophononic metamaterials

Bing Li,[1] K. T. Tan,[1] and Johan Christensen[2,*]
[1]*Department of Mechanical Engineering, The University of Akron, Akron, Ohio 44325-3903, USA*
[2]*Instituto Gregorio Millan Barbany, Universidad Carlos III de Madrid, ES-28916 Leganés, Madrid, Spain*
(Received 13 February 2017; published 12 April 2017)

Our research presents theoretical and numerical investigations of the dynamics and thermal transport properties in various locally resonant nanophononic metamaterials. Using finite element analysis, we show that the hybridization between the local resonances of the branched nanopillars and the bulk phonon modes of the host nanostructure can alter the phonon dispersion spectrum and greatly reduce the group velocities, leading to significant thermal conductivity reduction. According to the configuration of the periodic nanostructure, we propose a cantilever-in-mass model to theoretically analyze and control the resonance hybridization band. The influence of nanopillar number and size on the resonance hybridization frequency is systematically explored by both theoretical analysis and numerical simulation. Excellent agreement between theoretical results and numerical simulations reveals that the locally resonant frequencies can be accurately predicted by the proposed analytical model. Remarkably, the thermal conductivity of the resonant branched nanostructure can be tailored close to zero at the vicinity of local resonances with flat dispersion curves.

DOI: 10.1103/PhysRevB.95.144305

I. INTRODUCTION

Tremendous effort has been devoted to control the heat flow using nanostructured materials due to their promising prospect and broad applications in energy conversion and flux manipulation [1,2]. One of the pivotal quests in thermoelectric material engineering is to reduce the thermal conductivity k by man-made nanostructures [3]. The most common approach to reducing the thermal conductivity is to enhance the phonon scattering at boundaries and interfaces in nanostructured materials such as superlattices, nanowires, or nanocomposites [4–7]. By virtue of various phononic scattering elements such as inclusions, holes, or interfaces incorporated into semiconducting materials, reduction of the mean free path is possible, which leads to lowering of the thermal conductivity. However, an open challenge in thermoelectric materials is to realize a significant reduction in thermal conductivity, but meanwhile without negative effect on electronic transport. Although superlattices and nanophononic crystals are robust candidates to alter the thermal properties, unfortunately most of these systems also have an undesired negative impact on the electrical conductivity and Ohmic heating, which restrains the thermoelectric performance [8–10].

Different from the common route, an emerging concept of nanophononic metamaterials (NPMs) at the nanoscale has been proposed recently to circumvent this restriction [11]. A periodic array of nanopillars is built on the surface of a host membrane. This configuration of branched nanowire makes the nanopillars exhibit numerous local resonances. Hybridizing with the bulk phonon modes of the host nanostructures, the local resonances in NPMs directly modify the phonon dispersion relation and reduce the average group velocity. Without relying on the inclusion of phonon scattering, the resonance hybridization in NPMs can reduce the thermal conductivity, and meanwhile does not cause undesirable obstruction to the electron transport and thermoelectric conversion efficiency. Analogous anomalous resonance phonon reflection by periodic resonator chains in connection with heat transport in branched nanowires has been previously discussed by Kosevich [12]. Based on the phonon dispersion spectrum obtained by the atomic-scale lattice dynamics (LD) calculations, Davis and Hussein demonstrated that nanopillared films reduce the thermal conductivity of a uniform film by a factor of 2 [11]. Using molecular dynamics (MD) simulations, Xiong *et al.* [9], Wei *et al.* [13], and Honarvar and co-workers [10,14] also verified the thermal conductivity reduction induced by the resonance hybridizations. Xiong *et al.* [9] proposed a further combination of the local resonance and scattering effects to slow down the thermal transport at both low- and high-frequency ranges. Honarvar *et al.* [14] investigated the influence of size parameters on the performance of thermal conductivity reduction induced by the local resonance. Iskandar *et al.* [8] presented an experimental verification of the change of thermodynamic properties of NPMs induced by phonon hybridization effects.

These recent findings on NPMs are still at the preliminary conceptual design stage. Little work about the analytical model of this emerging nanostructure has been reported. In this work, we report a theoretical model to analyze the resonance hybridization mechanisms in various branched nanowires. The dynamics and thermal transport properties in these locally resonant nanostructures are systematically investigated. The effect of nanopillar number and dimension on the resonance hybridization is theoretically and numerically discussed where excellent agreements between theoretical results and numerical simulations are obtained at the low-frequency range. Particularly we report on near-zero thermal coefficients at local resonances with flat dispersion curves.

II. RESONANCE HYBRIDIZATION AND ANALYTICAL MODEL

A. Phonon dispersion relations

To tailor the thermal conductivity in NPMs, we first investigate the phonon dispersion spectra of various branched nanowires using the finite element method (FEM). The sketch

*johan.christensen@gmail.com

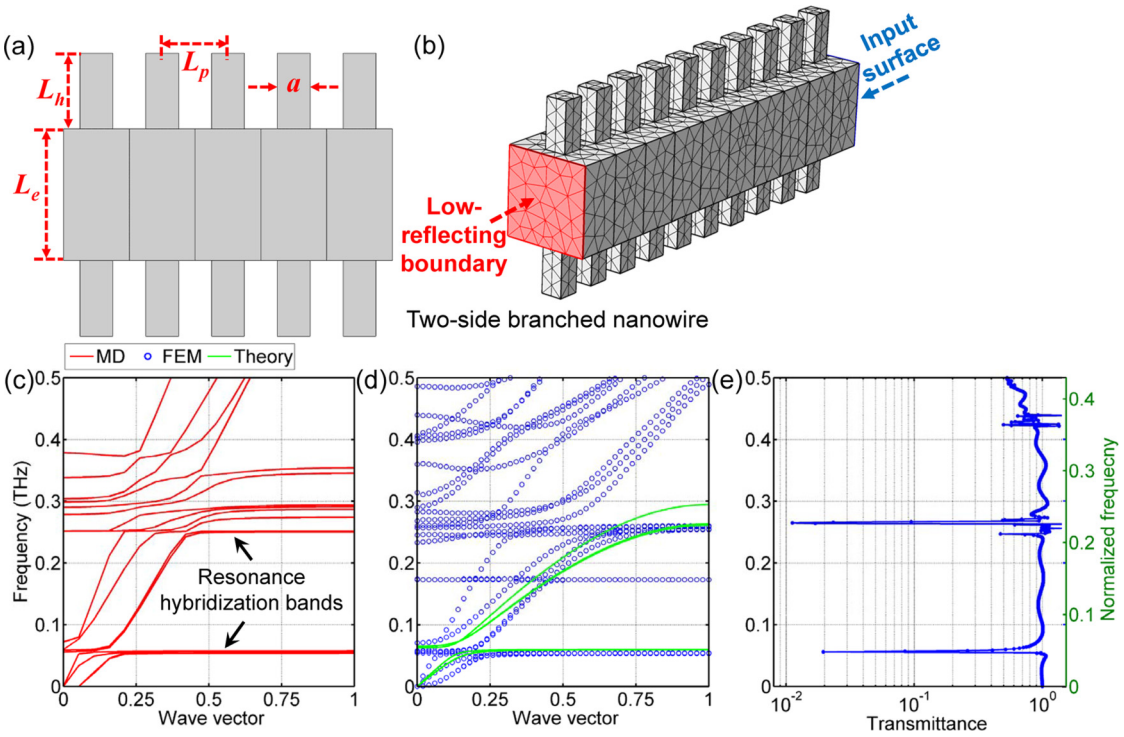

FIG. 1. (a) Side view of a two-side branched nanowire and (b) 3D FEM model after meshing. Phonon dispersions obtained by (c) MD calculation [9] and (d) FEM simulation (green curves correspond to theoretical predictions). (e) Transmittance-frequency profile in a two-side branched nanostructure consisting of ten unit cells.

of a two-side branched periodical nanowire is shown in Fig. 1(a). For each periodic unit cell, the cross section of the host nanowire is a square with an edge length of L_e. The cross section of each branched nanopillar is a square with a pillar width a. The height of each nanopillar is L_h. The thickness of each unit cell is L_p. The phonon dispersion for a two-side branched silicon nanowire has been obtained by MD simulations in Ref. [9] and is shown here in Fig. 1(c), where $L_e = 4.34\,\text{nm}$, $L_p = 2.17\,\text{nm}$, $L_h = 3.26\,\text{nm}$, and $a = 1.085\,\text{nm}$. The phonon spectrum for a same-sized three-dimensional (3D) continuum model of nanowire built by a commercial FEM software, COMSOL MULTIPHYSICS, is calculated in this research and depicted in Fig. 1(d). The boundary condition of Floquet periodicity is applied to the periodical nanoscale unit cell to evaluate the dispersion relations by the Bloch theorem [15]. The Young's modulus $E = 90\,\text{GPa}$, Poisson's ratio $\nu = 0.26$, and density $\rho = 5600\,\text{kg/m}^3$ are utilized in the FEM model [16]. A normalized frequency $f_N = L_p/\lambda$ is introduced to evaluate the comparison between MD and FEM calculations [see the right y axis in Fig. 1(e)]. λ is the wavelength and is expressed as $\lambda = c_t/f$, where $c_t = \sqrt{G/\rho}$ and G is the shear modulus, $G = E/[2(1+\nu)]$.

It is shown from Figs. 1(c) and 1(d) that except for a flat band around 0.17 THz, the phonon dispersion emerging from the FEM calculations matches very well with that obtained by the MD simulations in the low-frequency range (0–0.3 THz), where the wavelength is much larger than the size of a periodic unit cell. The first two main resonance hybridization bands (around 0.06 and 0.26 THz) induced by the local resonances of nanopillars are clearly observed in the phonon spectra calculated by both sets of simulations. In addition, the theoretical dispersion curves for this periodical nanostructure are also calculated and depicted in Fig. 1(d) (solid green lines) based on an equivalent spring mass-in-mass model, where the material properties are utilized to obtain the equivalent spring stiffness and mass. It is observed that the first resonance hybridization band in the theoretical dispersion spectrum agrees well with the numerical calculations, but the flat band around 0.17 THz is not predicted by theoretical analysis, either. The details relevant to the theoretical analysis and various flat bands will be discussed in the following section.

To explore the effect of resonance hybridization on the phonon transport, a finite-size nanostructure consisting of ten two-side branched unit cells is constructed and the FEM model after meshing is illustrated in Fig. 1(b). A low-reflecting boundary condition is applied to one end surface of this nanostructure to avoid the wave reflection while the other end surface is input by a time harmonic excitation at a sweep frequency range. The output dynamic response at the surface next to the low-reflecting boundary is captured, and the transmittances along the input direction at different frequencies are calculated by the ratio of output displacement to input displacement. As distinctly shown in Fig. 1(e), the transmittance has two obvious band gaps at the frequency ranges of resonance hybridization. The blocking effect of resonance hybridization on the phonon transport is verified.

B. Cantilever-in-mass model

To theoretically investigate the resonance hybridization, we propose a cantilever-in-mass model to describe the one-

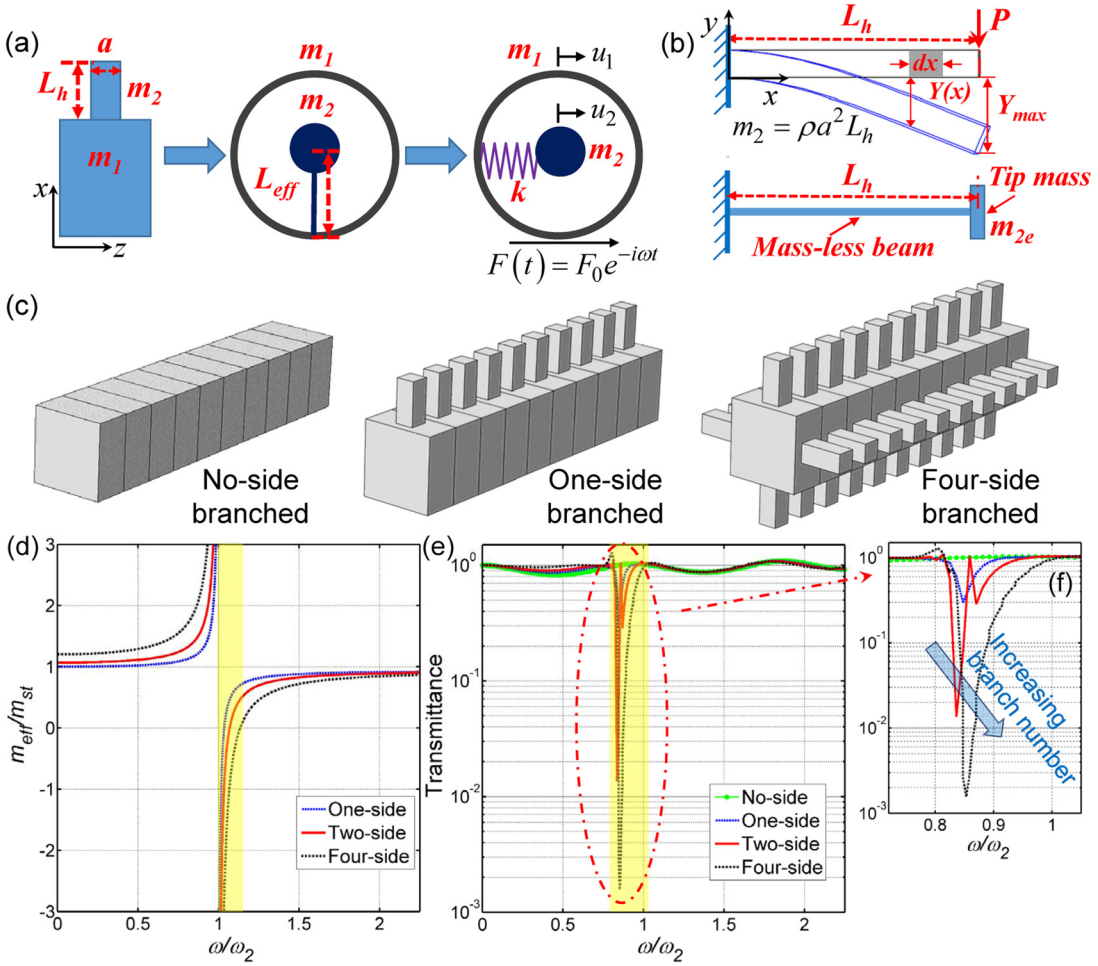

FIG. 2. (a) Equivalent cantilever-in-mass and mass-in-mass models for a one-side branched nanowire. (b) Deflection distribution of a cantilever beam and a discrete beam-tip mass model. (c) 3D FEM models, (d) theoretical normalized mass-frequency profiles and (e) numerical transmittance-frequency profiles for various branched nanostructures. (f) An enlarged view of the transmittance band gap.

side branched nanowire. As illustrated in Fig. 2(a), the host nanowire can be represented by an outer mass of m_1, and the side branched nanopillar can be enacted by a massless cantilever beam with an effective length of L_{eff} and an inner mass of m_2. The values of m_1 and m_2 can be calculated by the density and relevant volume; i.e., $m_1 = \rho L_e^2 L_p$ and $m_2 = \rho a^2 L_h$. We can further transform this cantilever-in-mass model into a classic spring mass-in-mass model. In the cantilever-in-mass model depicted in Fig. 2(a), we use Euler-Bernoulli beam theory to calculate the deflection of the beam [17]. Then, based on the deflection, we derive the equivalent spring stiffness of the cantilever beam as $k = 3EI_z/L_{\text{eff}}^3$, where I_z is the moment of inertia about the bending z axis or y axis, and $I_z = a^4/12$ [18]. On the basis of the spring mass-in-mass model [see Fig. 2(a)], we can obtain the equations of the motion for the outer and inner "masses" under a longitudinal harmonic force excitation as

$$F + k(u_2 - u_1) - m_1 \frac{d^2 u_1}{dt^2} = 0,$$
$$k(u_1 - u_2) - m_2 \frac{d^2 u_2}{dt^2} = 0. \quad (1)$$

Substituting $F(t) = F_0 e^{-i\omega t}$ and $u_j(t) = U_j e^{-i\omega t}$, $j = 1,2$ into Eq. (1), we obtain

$$F_0 + \left(m_1 + \frac{\omega_2^2 m_2}{\omega_2^2 - \omega^2}\right)\omega^2 U_1 = 0, \quad (2)$$

where ω is the input frequency and $\omega_2 = \sqrt{k/m_2}$ is the locally resonant frequency of the internal resonator [19,20]. If the unit cell of a one-side branched nanowire is further represented by a single effective mass m_{eff1}, we can calculate the effective mass using Eq. (2) as

$$m_{\text{eff1}} = m_1 + \frac{\omega_2^2 m_2}{\omega_2^2 - \omega^2}. \quad (3)$$

Using the equivalent spring stiffness and mass of the cantilever beam, we can describe the locally resonant frequency ω_2 as

$$\omega_2 = \sqrt{\frac{Ea^2}{4L_{\text{eff}}^3 \rho L_h}}. \quad (4)$$

The effective length L_{eff} can be approximately estimated based on the continuum beam theory and dynamic analysis

[17,21]. Considering a uniform cantilever beam subjected to a point load P at the free end, as depicted in Fig. 2(b), the deflection distribution along the beam, $Y(x)$, is given as

$$Y(x) = \frac{Px^2}{6EI_z}(3L_h - x) = \frac{Y_{\max}}{2L_h^3}(3L_h x^2 - x^3), \quad (5)$$

where $Y_{\max}$ is the deflection at the free end and $Y_{\max} = PL_h^3/(3EI_z)$. The length of the beam is L_h, and the width of the square cross section is a. Using Eq. (5), the velocity variation for the small element dx at distance x [see the shaded region in Fig. 2(b)] is given by

$$V(x) = \frac{(3L_h x^2 - x^3)}{2L_h^3}\dot{Y}_{\max} = \frac{V_{\max}}{2L_h^3}(3L_h x^2 - x^3). \quad (6)$$

The maximum value for the kinetic energy of the small element can be obtained as

$$dK = \frac{1}{2}\rho a^2\left[\frac{V_{\max}}{2L_h^3}(3L_h x^2 - x^3)\right]^2 dx. \quad (7)$$

For the whole uniform beam, the maximum kinetic energy is expressed as

$$\begin{aligned} K_{\max} &= \frac{1}{2}\int_0^{L_h} \rho a^2\left[\frac{V_{\max}}{2L_h^3}(3L_h x^2 - x^3)\right]^2 dx \\ &= \frac{1}{2}\left(\frac{33}{140}\rho a^2 L_h\right)V_{\max}^2. \end{aligned} \quad (8)$$

When a cantilever beam is subjected to free vibration, the system can be considered as a discrete system as illustrated in Fig. 2(b). The beam is treated as a massless cantilever beam with the same length of L_h, but the whole beam mass is concentrated as an equivalent tip mass of m_{2e} at the free end. For this equivalent system, the maximum kinetic energy equation is written as

$$K_{\max} = \tfrac{1}{2}m_{2e}V_{\max}^2. \quad (9)$$

According to Eqs. (8) and (9), the equivalent tip mass is approximately calculated as $m_{2e} = 0.24m_2$, and the natural frequency of the discrete system can be described as $\omega_{2e} = \sqrt{1.06Ea^2/(L_h^3\rho L_h)}$. Comparing the natural frequency with Eq. (4), the effective length L_{eff} in the cantilever-in-mass model can be estimated as $L_{\text{eff}} = 0.62L_h$.

Similarly, for the two-side branched and four-side branched nanowires as shown in Fig. 2(c), we can utilize analogous cantilever-in-mass and mass-in-mass models to deduce the equations of motion. For two-side branched nanowire,

$$F_0 + \left(m_1 + \frac{2\omega_2^2 m_2}{\omega_2^2 - \omega^2}\right)\omega^2 U_1 = 0. \quad (10)$$

For four-side branched nanowire,

$$F_0 + \left(m_1 + \frac{4\omega_2^2 m_2}{\omega_2^2 - \omega^2}\right)\omega^2 U_1 = 0. \quad (11)$$

The relevant effective mass m_{eff2} and m_{eff4} for the two-side branched and four-side branched nanowires can be obtained, respectively, as

$$m_{\text{eff2}} = m_1 + \frac{2\omega_2^2 m_2}{\omega_2^2 - \omega^2}, \quad m_{\text{eff4}} = m_1 + \frac{4\omega_2^2 m_2}{\omega_2^2 - \omega^2}. \quad (12)$$

Using Eqs. (3) and (12), we can plot the effective mass-frequency profiles for various side branched nanowires, as presented in Fig. 2(d). The total mass $m_{st} = m_1 + m_2$ and the frequency ratio ω/ω_2 are utilized for normalization. It is clearly shown that the effective mass is negative when the input frequency is close to the locally resonant frequency of the cantilever beam. The frequency band of the negative mass (shaded region) is enlarged with the increase of side branched nanopillars. The relevant transmittances for various side branched nanostructures consisting of ten unit cells [see Fig. 2(c)] are numerically calculated and compared in Fig. 2(e). The sweep frequency is normalized by the theoretical resonance frequency of ω_2. Compared with the no-side branch nanowire, side branched nanopillars lead to a band gap around the theoretical locally resonant frequency of ω_2, which blocks the phonon transport. An enlarged view of the transmittance band gap is shown in Fig. 2(f). It is clearly observed that the band gap becomes wider and deeper when we increase the number of branches, which matches very well with the theoretical prediction.

It is noticed in Fig. 2(f) that the predicted locally resonant frequency of ω_2 is a little higher than the numerical band gap. There are two main reasons for this overestimation. Firstly, the length-to-width ratio of the nanopillars discussed in this research is relatively small, where $L_h/a < 10$. The continuum beam theory used here is more suitable for a thin and long beam. Secondly, the boundary condition for the clamped end of the nanopillar is considered as a completely clamped connection in the proposed cantilever-in-mass model. However, the host nanostructure in the numerical simulations is not a completely fixed "ground." The slight simplification on the boundary condition may also overestimate the resonance frequencies. Therefore, to enhance the accuracy, a weight factor ζ $(0 \leqslant \zeta < 0.05)$ is introduced and the effective length is further expressed as $L_{\text{eff}} = [0.62/(1-\zeta)^2]L_h$. In the following discussion, ζ is taken as 0.035.

III. RESULTS AND DISCUSSION

A. Control of resonance hybridization

To more deeply understand the mechanisms of phonon resonance hybridization, we calculated the phonon dispersion spectra of different kinds of side branched structures. The comparisons of dispersion relations between host nanowire and various side branched nanowires are exhibited in Figs. 3(a)–3(d), respectively. The height of the branched nanopillar used here is $L_h = 3\,nm$. The comparison illustrates that the periodical nanopillars built on the surface of the host structure modify the original phonon spectrum and generate a series of flat resonant hybridization bands. We also find that adding additional branches enlarges the number of flat hybridization bands. The resonant modes at several representative frequencies are snapshot to visually present the coupling and

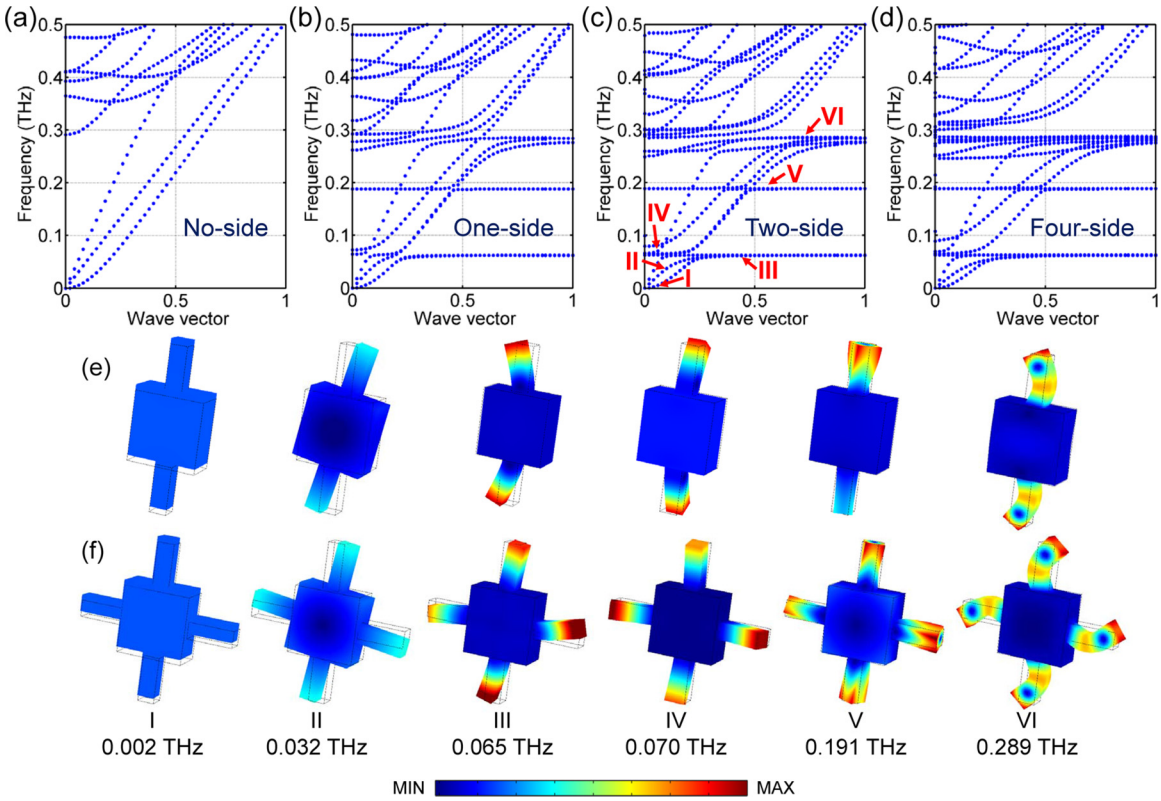

FIG. 3. (a) Phonon dispersion in the frequency range [0, 0.5] THz for (a) the host nanostructure (b) one-side, (c) two-side, and (d) four-side branched nanostructures. Various resonance modes at the frequencies of I–VI for (e) a two-side and (f) a four-side branched nanowire.

hybridization effect between the host and branched structures. We chose six representative frequencies within or outside the resonance hybridization bands [see Fig. 3(c), I–VI], and captured the relevant resonance modes for the two-side and four-side branched nanowires, as illustrated in Figs. 3(e) and 3(f), respectively. Below the hybridization bands (I and II), the resonance modes resemble a propagating phononic response. However, within the flat bands (III and IV), the branched nanopillars exhibit distinct resonant profiles whereas the host wire does not confine any vibrations. In other words, the phononic modes are localized within the nanopillars alone. Strong resonance coupling and hybridization between host structure and nanopillars occur around the flat bands and result in a distinct reduction in group velocity.

In addition, the vibration modes at the other two higher-order flat bands (V and VI) are also discussed. The corresponding resonance mode at point V shows a distinct localized twisting motion that we have not been able to capture by the theoretical analysis and MD calculations as we discussed in Figs. 1(c) and 2(d). We understand this by the superior degrees of freedom of mechanical motions in FEM 3D modeling as compared to simulations based on MD calculations and lumped equivalent models. As visualized in Figs. 3(e) and 3(f), the resonance hybridization around the frequency VI is induced by the second bending mode of the nanopillars. The massless beam and lumped mass model used in this research is a single degree of freedom (DOF) system. It is therefore not adequate to predict the torsional and higher-order transverse vibration. A FEM-based multiple-DOF system [22] or the dynamic Euler-Lagrange equations [21] for a cantilever beam can be further applied for the approximate estimation of the higher-order resonance hybridization bands (see the Appendix).

A series of models with various nanopillar dimensions is further investigated to discuss the effect of geometric tuning of the resonance hybridization band, and also to verify the reliability of the theoretical model. As shown in Fig. 4, we predict the change of the first hybridization band with

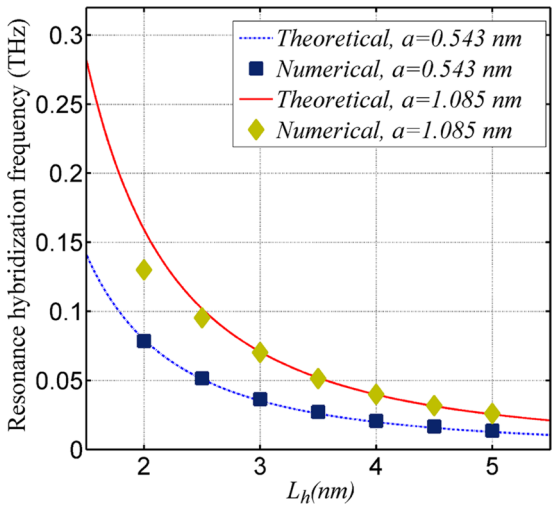

FIG. 4. Comparisons between theoretical and numerical resonance hybridization frequencies for branched nanostructures with different dimensions of nanopillars.

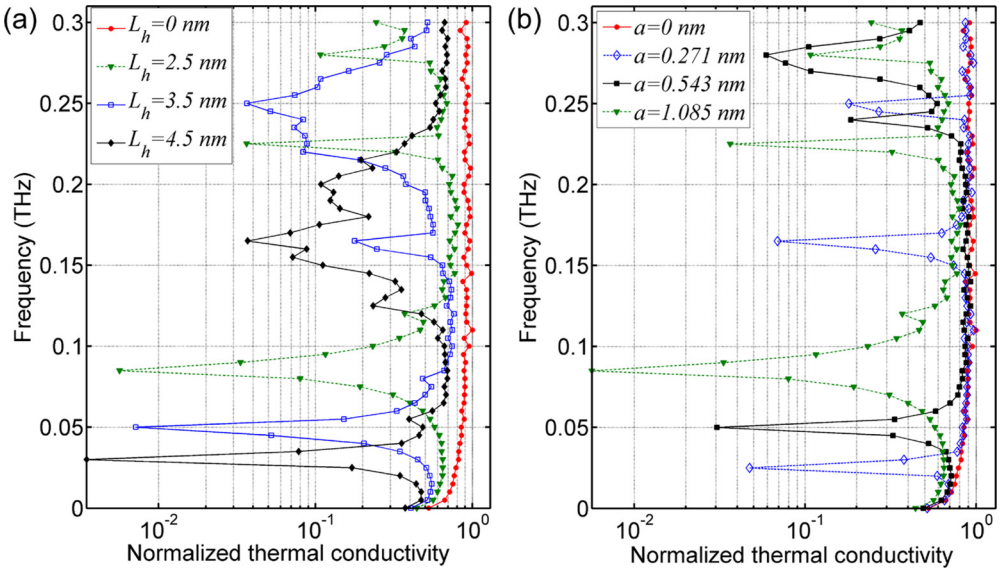

FIG. 5. Comparison of thermal conductivities as a function of frequency for a host nanowire and (a) branched nanowires with various heights of L_h and (b) various pillar widths of a.

the pillar height L_h and the pillar width a. We observe from Fig. 4 that the locally resonant frequency of the first hybridization band downshifts with the increase of nanopillar height. As the expression for the resonance suggests, enlarging the pillar width a also increases the resonance frequency. To verify the theoretical results, we numerically calculated the hybridization bands using a series of FEM models and compared them with theoretical values in Fig. 4. It is clearly illustrated that numerical results agree very well with the theoretical analysis, especially at the low-frequency range. It is, therefore, demonstrated that the theoretical model is very effective to analyze the locally resonant frequency of the branched nanopillars. The relevant resonance hybridization bands can be theoretically controlled and modified by the proposed cantilever-in-mass model.

B. Control of thermal conductivity

To offer direct evidence to the influence of resonance hybridization on the reduction of the thermal conductivity, we calculate and compare the thermal conductivities of the host and branched nanostructures using the Callaway-Holland (CH) model [23,24], where thermal conductivity T_c is expressed as

$$T_c = \frac{1}{L_p \pi} \sum_{\gamma} \int_0^{\pi/L_e} C(\kappa,\gamma) v_g^2(\kappa,\gamma) \tau(\kappa,\gamma) \kappa \, d\kappa, \qquad (13)$$

where C, v_g, τ, κ, and γ are specific heat, group velocity, scattering time, wave number, and branch index, respectively. The specific heat is written as $C(\kappa,\gamma) = k_B[\hbar\omega(\kappa,\gamma)/k_B T]^2 f(\kappa,\gamma)$, where k_B, $\hbar$, T, and ω are the Boltzmann constant, reduced Planck's constant, temperature, and the frequency, respectively, and $f(\kappa,\gamma) = e^{\hbar\omega(\kappa,\gamma)/k_B T}/[e^{\hbar\omega(\kappa,\gamma)/k_B T} - 1]^2$. The group velocity can be calculated by the derivation of the dispersion curve as $v_g(\kappa,\gamma) = \partial\omega(\kappa,\gamma)/\partial\kappa$. The scattering time is expressed as $\tau(\kappa,\gamma) = [\tau_U(\kappa,\gamma)^{-1} + \tau_I(\kappa,\gamma)^{-1} + \tau_B(\kappa,\gamma)^{-1}]^{-1}$, where τ_U is umklapp scattering, τ_I impurity scattering, and τ_B boundary scattering, which can be obtained by $\tau_U(\kappa,\gamma)^{-1} = AT\omega^2(\kappa,\gamma)e^{-B/T}$, $\tau_I(\kappa,\gamma)^{-1} = D\omega^4(\kappa,\gamma)$, and $\tau_B(\kappa,\gamma)^{-1} = |v_g|/L$, respectively. L is the effective boundary scattering length, which is defined as $L = L_p/(1-p)$. p is a surface specularity parameter between 0 and 1. In this research, $p = 0, k_B = 1.381 \times 10^{-23}$ J K^{-1}, $\hbar = 1.055 \times 10^{-34}$ J s, and $T = 300$ K. The parameters A, B, and D are obtained empirically as $A = 4.14 \times 10^{-15}$ s/K, $B = 899$ K, $D = 1.32 \times 10^{-45} s^3$ [11].

We compute Eq. (13) by evaluating the group velocity spectrally out of the dispersion relations. In order to normalize T_c, we first compute for the case of a bare unstructured nanowire, $L_h = 0$, and use its maximal thermal conductivity as a reference for NPMs containing various heights L_h [see Fig. 5(a)]. The results observed from the comparison of thermal conductivities are remarkable thanks to the phononic localized modes of zero group velocity. It is concluded that compared with the host nanowire, the thermal conductivities of the branched nanostructures are close to zero around the flat resonance hybridization bands. These extraordinary low-thermal-conductivity bands, which depend on the dimensions of the branched nanopillars, can be controlled and modified as predicted by the theoretical model proposed in this work. We also explore how the nanopillar width influences the resonance hybridization bands in Fig. 5(b). As expected, when increasing the pillar width a we also increase the resonance hybridization frequency. The thermal conductivities around these bands are also close to zero. It is evident that the existence of resonance hybridizations has an inherent contribution to the reduction in thermal conductivities that can be tailored through the geometrical parameters of the NPMs as suggested by the theoretical prediction.

IV. CONCLUSIONS

In conclusion, we presented a theoretical and numerical investigation of the thermal conductivity of locally resonant

NPMs. For wavelengths that are larger than the geometrical parameters of the structured nanowire we show that MD computations can be reproduced by FEM calculations that compare qualitatively well to theoretical predictions. We demonstrated for the first time a theoretical cantilever-in-mass model to effectively analyze and control the resonance hybridization bands in side branched NPMs. On the basis of the proposed analytical model, the resonance frequency can be accurately predicted in the low-frequency range. The analytical insight that we acquired confirms that the hybridized local resonances of the branched nanopillars are a powerful approach to reduce the thermal conductivity to extremely low values. By modifying the resonator size the thermal conductivity of the NPMs can be further theoretically manipulated and tailored, which could be potentially significant in thermoelectric conversion.

ACKNOWLEDGMENTS

The authors would like to thank Shiyun Xiong and Sebastian Volz for fruitful discussions and for providing their MD data for comparison. K.T.T. acknowledges the Faculty Start-Up Grant support from The University of Akron. J.C. gratefully acknowledges financial support from the MINECO through a Ramón y Cajal grant (Grant No. RYC-2015-17156).

APPENDIX: HIGHER-ORDER RESONANCE HYBRIDIZATION

The higher-order flat bands in the phonon dispersion spectra of side branched NPMs are mainly induced by the higher-order local resonance of the nanopillars. We can apply dynamic Euler-Lagrange equations to approximately estimate these flat frequency bands. For a dynamic Euler-Bernoulli beam with a length of L_h and a square cross section (width of a), the following differential equation can be derived according to the Euler-Lagrange equation [21]:

$$\frac{d^4Y(x)}{dx^4} - \beta^4 Y(x) = 0, \quad \beta^4 = \frac{\rho a^2 \omega^2}{EI_z}. \tag{A1}$$

The deflection distribution along the beam, $Y(x)$, can be generally written as $Y(x) = c_1 \sin\beta x + c_2 \cos\beta x + c_3 \sinh\beta x + c_4 \cosh\beta x$ and $c_{1,2,3,4}$ are constant coefficients. For a cantilever beam, the boundary conditions are readily obtained as

$$\begin{aligned} Y(0) = 0, \quad \left.\frac{dY(x)}{dx}\right|_{x=0} &= 0, \\ \left.\frac{d^2Y(x)}{dx^2}\right|_{x=L_h} &= 0, \\ \left.\frac{d^3Y(x)}{dx^3}\right|_{x=L_h} &= 0. \end{aligned} \tag{A2}$$

Using Eqs. (A1) and (A2), the frequency equation is derived as

$$\cos\beta_n L_h \cosh\beta_n L_h + 1 = 0, \quad n = 1,2,3,\ldots. \tag{A3}$$

The first natural frequency of a cantilever beam, ω_{b1}, can be calculated according to $\beta_1 L_h$, and the higher-order natural frequency can be approximately estimated by $\omega_{bN} = (\beta_N L_h)^2 \sqrt{Ea^2/(12\rho L_h^4)}$, $N > 1$. However, the present NPM is made out of nanopillars of small length-to-width ratio which currently only gives a rough estimation of the hybridization modes at high frequencies. More efforts to acquire a better estimation of the higher-order modes are currently under way.

[1] D. G. Cahill, W. K. Ford, K. E. Goodson, G. D. Mahan, A. Majumdar, H. J. Maris, R. Merlin, and S. Phillpot, J. Appl. Phys. **93**, 793 (2003).
[2] D. G. Cahill *et al.*, Appl. Phys. Rev. **1**, 011305 (2014).
[3] D. M. Rowe, *Thermoelectrics Handbook: Macro to Nano* (CRC Press, Boca Raton, FL, 2005).
[4] T. C. Harman, P. J. Taylor, M. P. Walsh, and B. E. LaForge, Science **297**, 2229 (2002).
[5] G. Pernot *et al.*, Nat. Mater. **9**, 491 (2010).
[6] J. Y. Tang, H. T. Wang, D. H. Lee, M. Fardy, Z. Y. Huo, T. P. Russell, and P. D. Yang, Nano Lett. **10**, 4279 (2010).
[7] H. X. Han, L. G. Potyomina, A. A. Darinskii, S. Volz, and Y. A. Kosevich, Phys. Rev. B **89**, 180301 (2014).
[8] A. Iskandar, A. Gwiazda, Y. Huang, M. Kazan, A. Bruyant, M. Tabbal, and G. Lerondel, J. Appl. Phys. **120**, 095106 (2016).
[9] S. Y. Xiong, K. Saaskilahti, Y. A. Kosevich, H. X. Han, D. Donadio, and S. Volz, Phys. Rev. Lett. **117**, 025503 (2016).
[10] H. Honarvar and M. I. Hussein, Phys. Rev. B **93**, 081412 (2016).
[11] B. L. Davis and M. I. Hussein, Phys. Rev. Lett. **112**, 055505 (2014).
[12] Y. A. Kosevich, Phys. Usp. **51**, 848 (2008).
[13] Z. Y. Wei, J. K. Yang, K. D. Bi, and Y. F. Chen, J. Appl. Phys. **118**, 155103 (2015).
[14] H. Honarvar, L. Yang, and M. I. Hussein, Appl. Phys. Lett. **108**, 263101 (2016).
[15] L. Brillouin, *Wave Propagation in Periodic Structures* (Dover Publications, Mineola, NY, 1953).
[16] M. E. Levinshtein, S. L. Rumyantsev, and M. S. Shur, *Properties of Advanced Semiconductor Materials: GaN, AlN, InN, BN, SiC, SiGe* (John Wiley & Sons, Inc., New York, 2001).
[17] J. M. Gere and S. P. Timoshenko, *Mechanics of Materials* (PWS Publishing Company, Boston, 1997).
[18] A. Qureshi, B. Li, and K. T. Tan, Sci. Rep. **6**, 28314 (2016).
[19] K. T. Tan, H. H. Huang, and C. T. Sun, Appl. Phys. Lett. **101**, 241902 (2012).
[20] B. Li and K. T. Tan, J. Appl. Phys. **120**, 075103 (2016).
[21] L. Meirovitch, *Analytical Methods in Vibrations* (Macmillan Publishing Co., Inc, New York, 1967).
[22] A. Eddanguir and R. Benamar, in *Design and Modeling of Mechanical Systems* (Springer, Berlin, Heidelberg, 2013), p. 89.
[23] J. Callaway, Phys. Rev. **113**, 1046 (1959).
[24] M. G. Holland, Phys. Rev. **132**, 2461 (1963).